Ultrahigh Gain of a Vacuum-Ultraviolet Photodetector Based on a Heterojunction Structure of AlN Nanowires and NiO Quantum Dots

Mengting Liu,[1] Xianjie Wang,[1] Tai Yao,[2] Bin Fang,[3] Yiyong Wu,[4] Chengyue Sun,[4] Zhongming Zeng,[3] and Bo Song[1,5,*]

[1] *School of Physics, Harbin Institute of Technology, Harbin 150001, China*

[2] *Interdisciplinary Science Research Center, Harbin Institute of Technology, Harbin 150001, China*

[3] *Key Laboratory of Nanodevices and Applications, Suzhou Institute of Nano-tech and Nano-bionics, Chinese Academy of Science, Suzhou 215123, China*

[4] *School of Materials Science & Engineering, Harbin Institute of Technology, Harbin 150001, China*

[5] *National Key Laboratory of Science and Technology on Advanced Composites in Special Environments, Harbin Institute of Technology, Harbin 150001, China*

(Received 8 February 2020; revised manuscript received 30 April 2020; accepted 4 May 2020; published 16 June 2020)

Aluminum nitride (AlN) is a promising candidate for the manufacture of vacuum ultraviolet (VUV) photodetectors. However, its poor electrical conductivity limits its applications. Herein, a high-performance AlN nanowire (NW)-NiO quantum dot (QD) based VUV photodetector is constructed via a mixed-dimensional strategy. The formation of isolated nanoscale *p*-*n* heterojunctions greatly increases the concentration of photogenerated electrons, resulting in an ultrahigh photoconductive gain (9.96) in the AlN NW-NiO QD material, which is about 27-fold higher than that of AlN NW (0.368). In addition, the significant improvement in both photocurrent and response speed convincingly suggest the great potential of AlN NW-NiO QD based VUV photodetectors. Furthermore, the properties of these photodetectors in an irradiation environment are also evaluated here. It is found that AlN NW exhibits excellent anti-irradiation characteristics towards both electron and proton irradiation, while the AlN NW-NiO QD material also presents promising potential under low-dose electron irradiation. This study can be used as a guideline to design and fabricate high-performance VUV photodetectors based on wide-band-gap semiconductors coupled with other nanostructured systems.

DOI: 10.1103/PhysRevApplied.13.064036

I. INTRODUCTION

Ultraviolet (UV) photodetectors based on wide-band-gap semiconductors (WBGSs), with E_g values generally in the range of 3–6 eV, are arousing great interest in many fields, such as missile warning systems [1], space exploration [2], flame detection [3], secure communication [4], and biological or chemical analysis [5]. Various types of WBGS, including diamond (5.5 eV) [6], Ga_2O_3 (4.2–4.9 eV) [7], SiC (3.44 eV) [8], GaN (3.42 eV) [9], and ZnO (3.34 eV) [10–12], have been used to fabricate photodetectors with outstanding performances in the UV range. However, their narrow band gap (usually <6 eV) results in poor selectivity in the vacuum ultraviolet (VUV) range ($\lambda < 200$ nm), restricting the field of application. To overcome this problem, aluminum nitride (AlN), with a band gap of 6.2 eV, has attracted increasing attention due to its high breakdown field strength, high thermal conductivity ($\sim 3.4\,\mathrm{W\,cm^{-1}\,K^{-1}}$) [13,14], and excellent radiation resistance [15,16]. These properties make this compound an ideal candidate for the preparation of VUV photodetectors [17]. However, the intrinsic physical shortcoming of low carrier concentration in AlN [18] restricts its photoconductive gain. Hence, the development of AlN-based photodetectors with special morphologies is expected to enhance their photoelectric response. In contrast with bulk or film-based AlN photodetectors, the nanostructured counterpart, especially the one-dimensional AlN nanowire (NW) based detector will exhibit an improved photoelectric response characteristic. Since the NWs are associated with a high surface-to-volume ratio [19–21], vectorial charge separation and transfer [22–24], and a short lateral charge transport length [2], these will significantly improve the transport properties of the carriers. For instance, Zheng *et al.* showed the potential of AlN micro- or nanowire-based VUV photodetectors with a high quantum efficiency (QE) of 254% [25]. To overcome the intrinsic physical limitations of AlN, band-gap engineering, including heterogeneous atom doping or *p*-*n* heterojunctions, is studied [26–28]. Tran *et al.*

*songbo@hit.edu.cn

reported that the carrier concentration was increased by about 7 times in Mg-doped AlN NW [29]. Recently, Li *et al.* reported a Zn_2SnO_4/ZnO heterojunction photodetector, which showed 10 times higher photocurrent and responsivity [30]. By taking advantage of both nanostructures and heterojunctions simultaneously, it is possible to improve the gain further, which seems to be promising and challenging. Generally, since the unintentionally doped AlN is an *n*-type semiconductor, a *p*-type WBGS, such as nickel oxide (NiO, $E_g = 3.4$–4 eV) [31,32], chromium sesquioxide (Cr_2O_3, $E_g = 3.2$–3.4 eV) [33], or copper oxide (Cu_2O, $E_g = 2.17$–2.6 eV) [34], is thus required to form the heterostructure. Among these *p*-type semiconductors, NiO is selected in this study due to its high electrical properties, as well as excellent thermal and chemical stability [35].

Herein, the mixed-dimensional AlN NW-NiO quantum dot (QD) heterostructure is constructed, which achieves an excellent performance among all AlN-based VUV photodetectors, including ultrahigh photoconductive gain (9.96) and light-to-dark ratios (3.6×10^5). Further, the potential of AlN-based devices toward irradiation environment are carefully evaluated, which demonstrates the great stability of AlN-based VUV photodetectors, and displays the great potential of AlN NW-NiO QD based VUV photodetectors under low-dose electron irradiation. This study widens the available knowledge of the design and fabrication of photodetectors, especially for VUV optoelectronic applications based on WBGSs.

II. DISCUSSION

Single-crystal AlN NWs are prepared via the physical vapor transport (PVT) technique in a homemade radiofrequency-heated furnace (see Fig. 6 and experimental details in Appendix A). The X-ray diffraction (XRD) pattern (Fig. 7 in Appendix A) of the samples presents a series of peaks that allow to be identified as wurtzite AlN [2H phase crystal structure, "*abab*" stacking order, space group $P6_3mc$, and crystal structure in the inset of Fig. 1(c)]. This result is in agreement with the standard ICDD-PDF-2 card no. 01-073-7288. In this spectrum, no impurity phases or other secondary phases are detected. Furthermore, the Rietveld refinement based on the FULLPROF program [36] shows that the lattice parameters of the synthesized AlN samples are $a = 3.112$ Å and $c = 4.977$ Å. Both are in good agreement with the standard values of $a = 3.111$ Å and $c = 4.978$ Å. A scanning electron microscopy (SEM) image [Fig. 1(a)] of the sample with an enlarged view [the inset in Fig. 1(a)] reveals that AlN NWs are typical NWs with a characteristic diameter and length of 100–250 nm and 30–100 μm, respectively. The Raman characterization [Fig. 1(f)] of the samples further demonstrates that the NWs consist of the AlN crystal structure, with characteristic Raman modes located at 909.0, 889.1, 668.4, 656.3, 608.9, and 246.7 cm^{-1}, corresponding to the E_1 (LO), A_1 (LO), E_1 (TO), E_2 (high), A_1 (TO), and E_2 (Low) modes, respectively [37,38]. The transmission electron microscopy (TEM) image [Fig. 1(b)] and clear

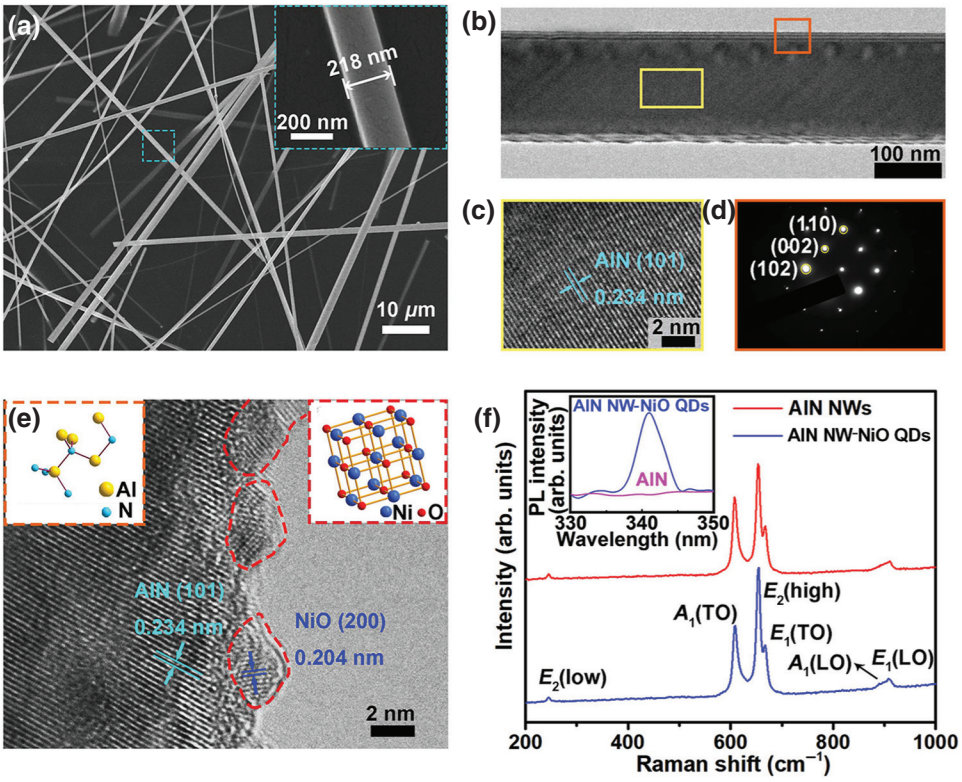

FIG. 1. Material characterization. (a) SEM image of the AlN NWs. Inset shows an enlarged view of the blue area. (b) TEM image, (c) HRTEM image, and (d) SAED pattern of the AlN NWs. (e) HRTEM image of the AlN NWs with NiO QDs. Insets show the molecular structures of AlN and NiO. (f) Raman spectra of AlN NWs and AlN NW-NiO QD material. Inset presents PL spectra of the NiO QDs and AlN NW-NiO QD material.

lattice high-resolution TEM (HRTEM) image [Fig. 1(c)] distinctly show that the obtained highly crystalline AlN NWs are defect-free. The 0.234 nm interplanar distance [Fig. 1(c)] measured corresponds to the hexagonal d_{101} values of AlN, which further confirms the formation of AlN. The Debye-Scherrer diffraction dots, which are visible in the selected-area electron diffraction (SAED) pattern [Fig. 1(d)] show the single-crystal nature of the AlN NWs. To construct the *p*-*n* heterojunction photodetectors, *p*-type NiO QDs [face-centered cubic, inset of Fig. 1(c)] are deposited onto the AlN NWs via the pulsed laser deposition (PLD) method (see Fig. 8 and experimental details in Appendix B). The TEM and HRTEM images (Fig. 9 and inset in Appendix B) show the presence of well-dispersed NiO QDs with sizes of 4–6 nm. Furthermore, the HRTEM image of the heterojunction in Fig. 1(e) clearly shows that the AlN NWs are tightly dotted with the NiO QDs for the hydric dimension structure combining one-dimensional NWs and zero-dimensional QDs. The presence of the NiO QDs cannot be detected via Raman characterization [Fig. 1(f)], probably due to their low content and poor crystallinity compared with that of the AlN NWs. To further verify the successful deposition of the NiO QDs, the photoluminescence (PL) spectra [the inset in Fig. 1(f)] of AlN NWs and the AlN NW-NiO QD material are recorded. It can be seen that no obvious PL peaks for the AlN NWs, ranging from 330 to 350 nm, are detected, but a broad peak located at 341 nm in the spectrum of the AlN NW-NiO QD material is observed. So, the PL peak located at 341 nm should be attributed to NiO QDs ($E_g = 3.63$ eV), with an average size of 5–7 nm [39]. The AlN NW-NiO QD based photodetectors are fabricated via the photolithography process schematically shown in Figs. 2(a)–2(f). In a typical run, a large number of AlN NWs and NiO QDs are mixed with a solution consisting of 99% alcohol and 1% deionized water and then dispersed via an ultrasonic treatment for 30 min. Successively, the solution is deposited onto a silicon oxide (SiO_2) substrate and the AlN NWs and NiO QDs tightly adhere to the SiO_2 wafer after volatilization of the solution [Fig. 2(a)]. The photoresists are then deposited onto the SiO_2 wafer and covered with a metal mask [Fig. 2(b)]. The sample is exposed to ultraviolet illumination to dissolve the redundant photoresists. A 150-nm-thick Au film is then deposited onto the SiO_2 substrate via electron-beam evaporation [Figs. 2(c) and 2(d)]. After lifting off the rest of the photoresists [Fig. 2(e)], an effective electrode consisting of the Au pattern on the SiO_2 wafer is obtained [Fig. 2(f)]. In this way, the ohmic contact in the

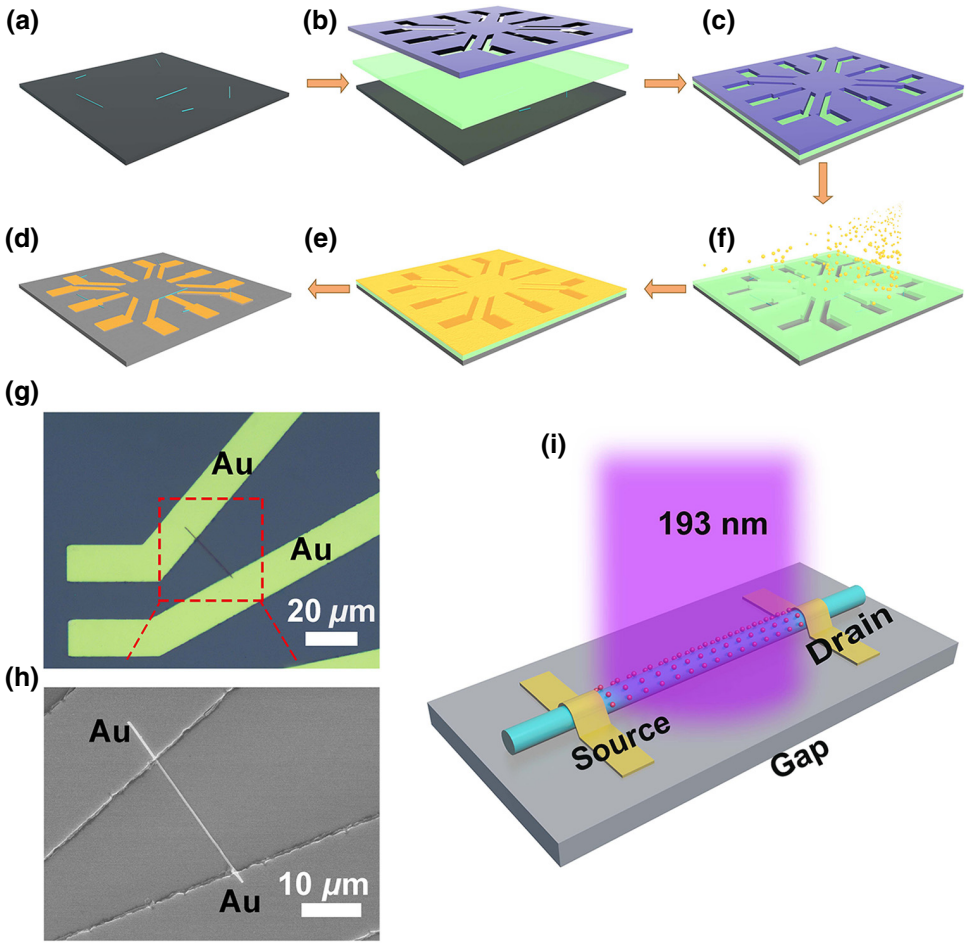

FIG. 2. (a)–(f) Preparation of the electrodes via photolithography. (g) Optical image, (h) SEM image, and (i) schematic diagram of the photodetector device.

AlN NW-NiO QD material used in these experiments can be fabricated. The optical [Fig. 2(g)] and SEM [Fig. 2(h)] images of the device show that the two Au electrodes, serving as the source and drain electrodes, respectively, are at a spacing distance of 20 μm and connected via the AlN NW-NiO QD material. Figure 2(i) shows the setup under UV illumination. Similarly, the AlN NW based photodetectors are also fabricated via the same process as that mentioned above.

To evaluate the performance of a photodetector, two key parameters, namely, the photoconductive gain (G) and the spectral responsivity (R_λ) [40,41], should be considered; these parameters are defined as follows:

$$G = \frac{hc}{q\lambda} R_\lambda \cong \frac{1.24}{\lambda} R_\lambda, \tag{1}$$

$$R_\lambda = I_{\text{ph}}/P_{\text{opt}}. \tag{2}$$

Here, h is Planck's constant, c is the speed of light, q is the elementary charge, λ is the wavelength of irradiated light, I_{ph} is the photocurrent (in A), and P_{opt} is the incident light intensity [42,43]. When compared with the AlN NW [Fig. 3(a)], the AlN NW-NiO QD material [Fig. 3(d)] shows a significant enhancement in its photocurrent, which increases from 8.47 to 216.39 nA upon illumination with a VUV source of 193 nm. Moreover, a 27-fold increase is achieved in the photoconductive gain, which measures to be 0.368 in AlN NW and 9.96 in the AlN NW-NiO QD material. The dramatic increase in the photocurrent and photoconductive gain may be attributed to modification of the NiO QDs, which form numbers of isolated nanoscale p-n heterojunctions with the AlN NW. On the contrary, the I_{dark} of both the AlN NW-NiO QD material and AlN NW have similar values, indicating that the isolated nanoscale p-n heterojunctions have a limited influence on the internal transport characteristics of the AlN NW. Besides, the light-to-dark current ratio ($I_{\text{light}}/I_{\text{dark}}$) and the specific detectivity [$D^* = R_\lambda/(2eI_{\text{dark}}/S)^{1/2}$] are also critical parameters, which influence the photoelectric response and the detectable signal threshold of the photodetectors, respectively [44]. The $I_{\text{light}}/I_{\text{dark}}$ values of the photodetectors obtained without and with additional QDs are 1.6×10^3 and 3.6×10^5, respectively, and the D^* values are 1.84×10^5 and 5×10^6 Jones, respectively. Clearly, both obtained photoconductive gain and $I_{\text{light}}/I_{\text{dark}}$ of the AlN NW-NiO QD material are superior to that of other AlN-based photodetectors (Table I). Moreover, the photocurrent of the AlN NW increases monotonically with increasing V_{DS} from −40 to 40 V, with a 5 V step [the inset of Fig. 3(a)]. Similar behavior can also be observed in the AlN NW-NiO QD material [the inset of Fig. 3(d)] due to their higher V_{DS}, which significantly improves the separation efficiency of the electron-hole pairs triggered by the illumination process. Herein, the optical response speed of AlN NW [Fig. 3(b)] and the AlN NW-NiO QD material [Fig. 3(e)], which refers to the time interval between

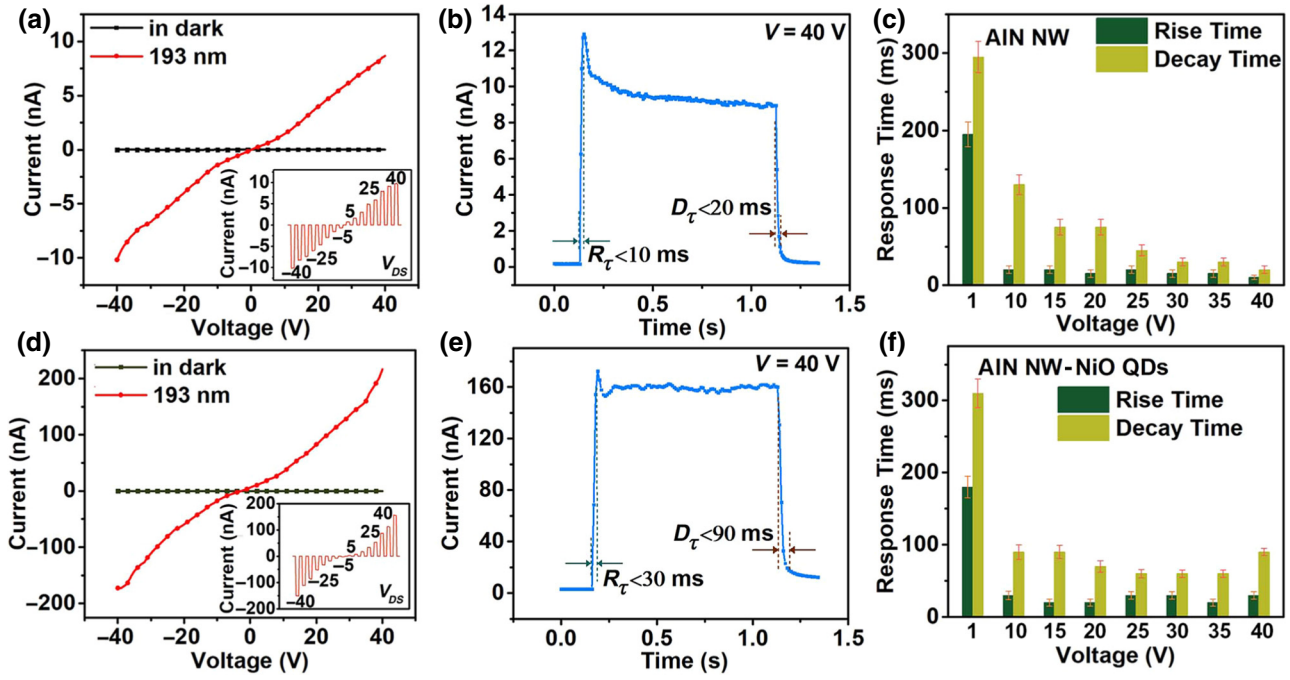

FIG. 3. Characterization of the performance of the photodetectors. I-V curves of (a) the AlN NW and (d) AlN NW-NiO QD material with and without 193 nm UV illumination. Insets show the photocurrent for various V_{DS} (in the −40 to 40 V range) with a step of 5 V. Time-dependent response of (b) the AlN NW and (e) AlN NW-NiO QD photodetectors, when a bias voltage of 40 V is applied. Rise time and decay time of (c) AlN NW and (f) AlN NW-NiO QD material as a function of the bias voltage.

TABLE I. Comparison between the photoelectric response performances of the AlN-based photodetectors measured in this work and in previous works.

Photodetector	Wavelength (nm)	Responsivity (A W^{-1})	Photoconductive gain	I_{light}/I_{dark} ratio	Rise time	Decay time	Detectivity (Jones)	Refs
AlN bulk	360	3.7	–	–	–	–	–	[66]
AlN epilayer	200	0.078	–	–	–	–	–	[67]
AlN film	202	0.08	–	–	–	–	–	[68]
Gr/AlN film/GaN	195	0.067			80 ns	0.4 ms		[69]
Gr/AlN film/ZnO	185	0.04			4 μs	1 ms		[70]
Gr/AlN film/Si	193	0.054			120 ns	2 ms		[71]
AlN micro- or nanowires	193	0.39	–	–	<0.1 s	<0.2 s	–	[25]
AlN nanowire	193	0.0573	0.368	1.6×10^3	<10 ms	<20 ms	1.84×10^5	This work
AlN NW-NiO quantum dots	193	1.55	9.96	3.6×10^5	<30 ms	<90 ms	5×10^6	This work

the rise (decay) in the 10%–90% (90%–10%) range of the peak value, is measured by repeatedly switching on and off the 193 nm laser. The rise and decay times for AlN NW are <10 and <20 ms, respectively, while in the AlN NW-NiO QD material they are <30 and <90 ms, respectively. Clearly, the response speed of AlN NW is faster than that of the AlN NW-NiO QD material. Generally, the response speed of the *p*-*n* junction photodetector should be faster than that of the photoconductive photodetector. However, the AlN NW-NiO QD material is still of photoconductive type, instead of *p*-*n* junction type, because isolated nanoscale AlN/NiO *p*-*n* junctions are located on the surface of AlN, and thus, the main carrier transport process occurs inside the AlN NW. Meanwhile, both AlN NW and the AlN NW-NiO QD material show comparable or rapider responses upon the fast switching of optical signals, relative to that of other AlN-based photoconductive photodetectors due to the high quality of AlN NW, but slower than those of AlN-based *p*-*n* junction photodetectors (Table I). To further determine how

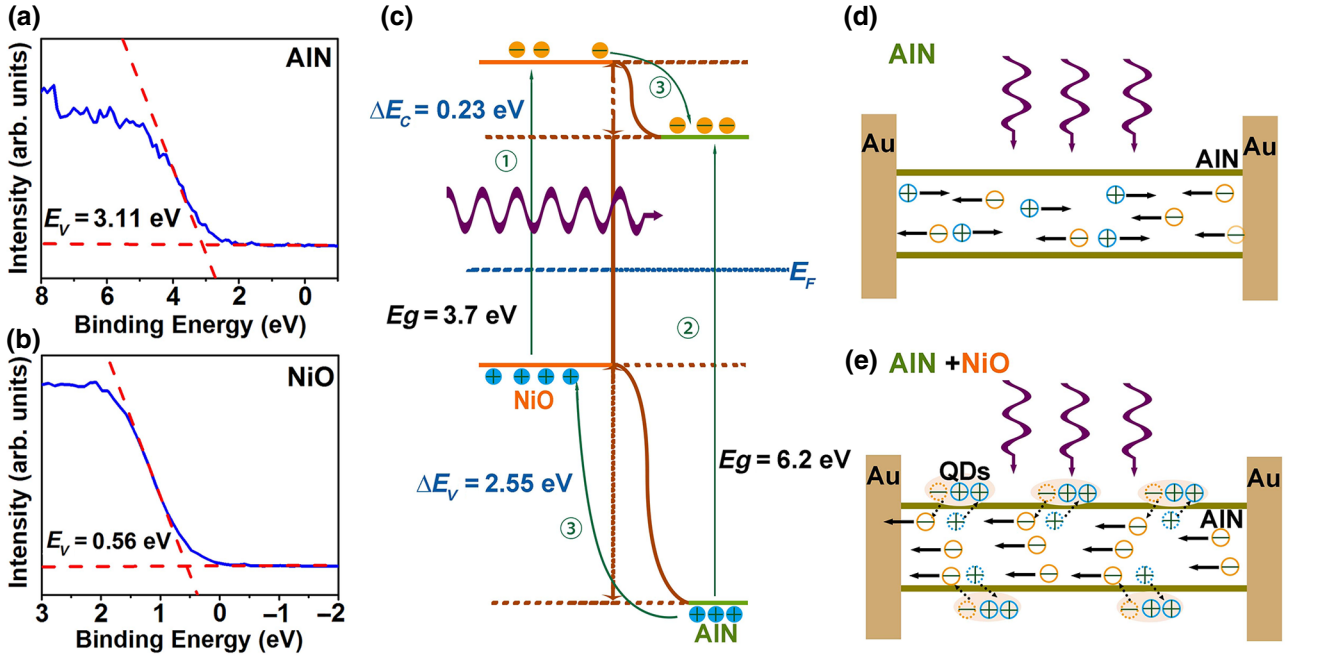

FIG. 4. VBM positions of (a) pristine AlN NW and (b) NiO QDs. (c) Energy-band diagram of the heterostructure at 193 nm, showing the photogenerated carrier-transport mechanism under illumination. Electron and hole transport mechanisms of (d) AlN NW and (e) AlN NW-NiO QD material under illumination.

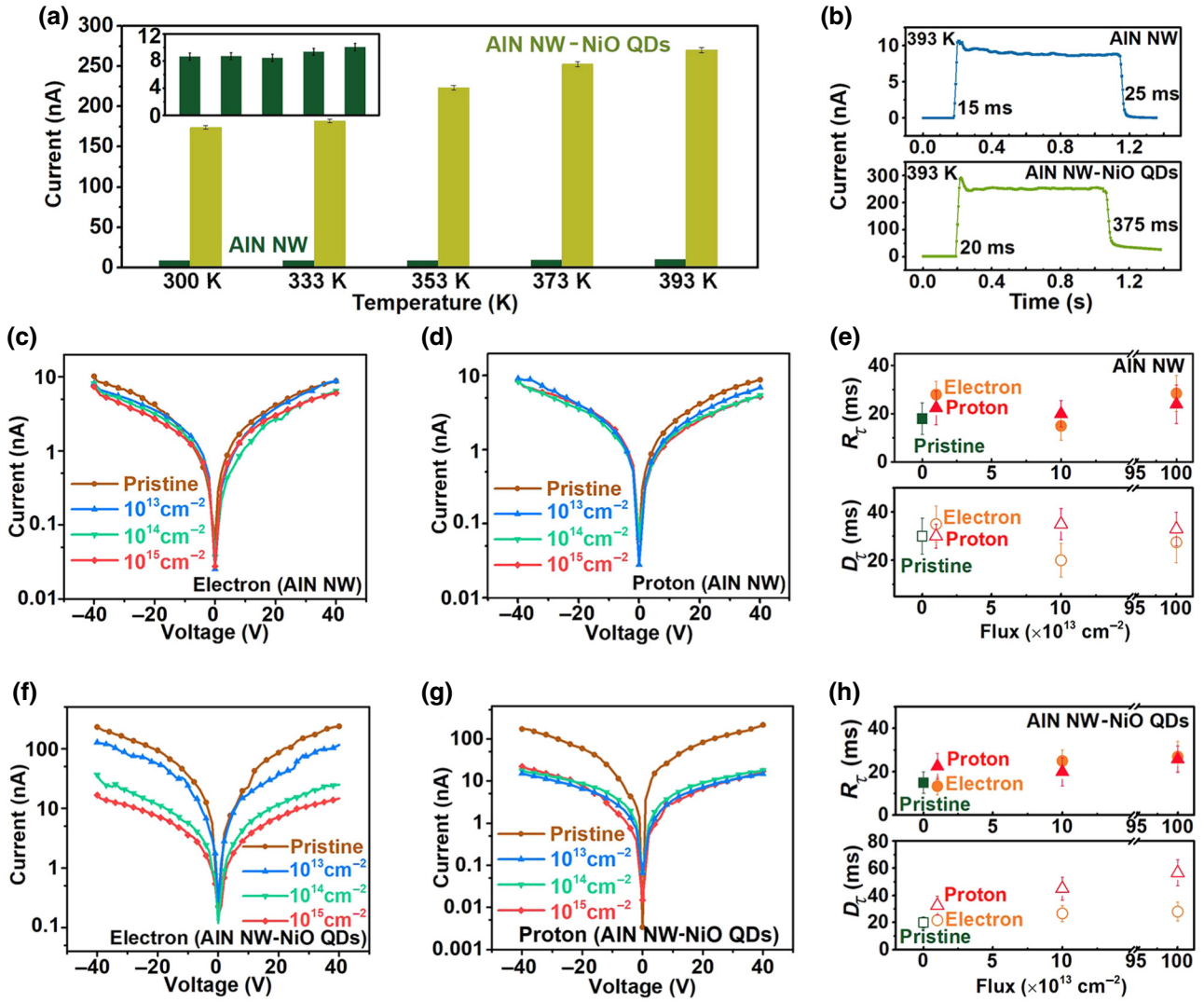

FIG. 5. (a) Photocurrent bar chart of AlN NW and AlN NW-NiO QD material at various temperatures from 300 to 393 K at 40 V. (b) Time-dependent photoelectric response of AlN NW (top) and AlN NW-NiO QD (bottom) photodetectors at 393 K. *I-V* measurements after (c) 170 keV electron irradiation and (d) 120 keV proton irradiation of AlN NW. (e) Response speed of AlN NW after irradiation with various fluxes at 40 V. *I-V* measurements after (f) 170 keV electron irradiation and (g) 120 keV proton irradiation for AlN NW-NiO QD material. (h) Response speed of AlN NW-NiO QD material after irradiation with various fluxes at 40 V.

V_{DS} affects the response speed, a series of measurements are performed in the V_{DS} range of 1–40 V [Figs. 3(c) and 3(f), as well as Fig. 10 in Appendix D). The obtained rise time and decay time under 1 V for AlN NW are (195.1 ± 10.4) and (295.6 ± 15.4) ms, respectively, while those for the AlN NW-NiO QD material are (180.1 ± 8.3) and (310.9 ± 17.2) ms, respectively. With an increase in V_{DS}, a faster response speed is achieved for both AlN NW and the AlN NW-NiO QD material. For AlN NW, the rise time rapidly drops down to the range from 10 to 25 ms, with a limited variation up to 40 V, while the decay time exhibits a monotonously decrease from (295.6 ± 15.4) to (20.4 ± 4.1) ms as a function of V_{DS}. Similarly, in the AlN NW-NiO QD material, the rise time displays a clear decrease from (180.1 ± 8.3) ms to the range from 15 to 35 ms with an increase of V_{DS}, while the decay time descends initially and then increases, with a minimum value of (60.2 ± 5.2) ms observed at 25 V, which is about one-fifth of that at 1 V. Herein, the improved response speed should be ascribed to the enhancement in carrier drift speed at higher V_{DS}.

To shed some light on the mechanism behind the improved performance, the energy band of the heterojunction is investigated. To identify the position of the energy level, the core levels (CLs) and the valence band photoemission (VBM) of the samples are measured by X-ray photoelectron spectroscopy (XPS, see Fig 11 and corresponding discussion in Appendix D). Via a linear

TABLE II. Specific parameters of response speed of AlN NW and AlN NW-NiO QD material at high temperature.

		333 K	353 K	373 K	393 K
AlN NW	R_τ (ms)	21.2 ± 4.3	20.3 ± 4.6	22.4 ± 4.5	15.3 ± 4.4
	D_τ (ms)	24.3 ± 4.5	25.3 ± 4.4	35.1 ± 5.4	26.1 ± 4.7
AlN NW-NiO QDs	R_τ (ms)	31.5 ± 5.4	29.3 ± 5.1	18.7 ± 4.8	18.6 ± 4.3
	D_τ (ms)	121.3 ± 7.1	124.7 ± 7.8	205.7 ± 12	374.7 ± 20.4

least-squares fit of the leading edge [45] of the valence band (VB) spectrum, the VBM locations of Al $2p$ and Ni $2p$ are identified at 3.11 eV [Fig. 4(a)] and 0.56 eV [Fig. 4(b)], respectively. Moreover, the valence band offset (VBO) and the conduction band offset (CBO) of the AlN NW-NiO QD material are calculated to be $\Delta E_V = 2.55$ eV and $\Delta E_C = 0.23$ eV, respectively, as follows:

$$\Delta E_V = (E_{\mathrm{Ni}\,2p} - E_{V\,\mathrm{NiO}})^{\mathrm{NiO}} - (E_{\mathrm{Al}\,2p} - E_{V\,\mathrm{AlN}})^{\mathrm{AlN}} - \Delta E_{\mathrm{CL}}, \quad (3)$$

$$\Delta E_C = \Delta E_V + E_g^{\mathrm{NiO}} - E_g^{\mathrm{AlN}}. \quad (4)$$

The energy-band diagram of the AlN NW-NiO QD material is presented in Fig. 4(c) to elucidate the carrier transport mechanism. When the NiO QDs are deposited onto the AlN NW, many isolated nanoscale p-n junctions, with a type II heterojunction band structure, are formed. The diffusion of carriers generates the built-in electric field, which results in a modification of the Fermi energy at equilibrium [46]. When the AlN NW-NiO QD material is irradiated with a 193 nm laser, a large number of electron-hole pairs, which rapidly migrate toward opposite directions, as driven by the built-in electric field, are generated. In short, three processes occur when the device is illuminated: 1) the photogenerated electrons in the NiO QDs jump from the VB to the CB; 2) meanwhile, partial electrons in the AlN NW absorb photons and jump to the CB, generating holes in the VB; and 3) subsequently, photogenerated electrons migrate from the CB of NiO to that of AlN, while partial holes migrate from the VB of AlN to that of NiO, due to the built-in electric field. These photogenerated electrons increase the electron concentration in AlN and the migration of photogenerated holes from AlN to NiO further increases the hole concentration in NiO. Thus, unlike AlN NW [Fig. 4(d)], for the AlN NW-NiO QD material, there is a hole-enrichment area in the NiO QDs and electron-enrichment regions in the AlN NW [Fig. 4(e)], which suppress the recombination of electron-hole pairs, leading to a remarkable increase in the photocurrent and a reduction of the response speed in the AlN NW after the deposition of NiO QDs.

To further verify the potential of AlN-based VUV photodetectors at high temperature, as expected, the photoelectric response characteristics are evaluated in the range from 300 to 393 K. Clearly, as shown in Fig. 5(a), the photocurrent of AlN NW decreases initially with increasing temperature from (8.47 ± 0.31) nA (300 K) to (8.44 ± 0.25) nA (353 K) and then increases to (10.07 ± 0.25) nA (393 K). Meanwhile, the photocurrent of the AlN NW-NiO QD material gradually rises from (216.39 ± 5.50) nA (300 K) to (269.75 ± 5.50) nA (393 K), suggesting excellent high-temperature performance and an outstanding stability of heterostructure-based photodetectors. In Figs. 12(a) and 12(b) (see in Appendix D), similar characteristics of the photocurrent can still be observed independent of V_{DS} [see insets of Figs. 12(a) and 12(b) in Appendix D]. For AlN NW and the AlN NW-NiO QD material, as the temperature increases, the scattered effects from lattice vibrations

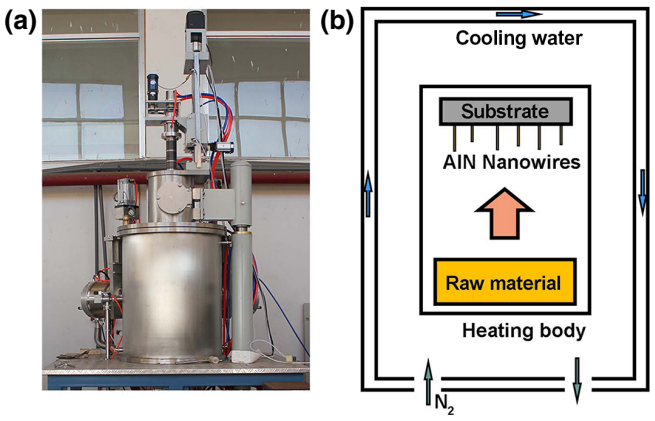

FIG. 6. (a) Photograph of PVT equipment. (b) Schematic diagram of PVT system.

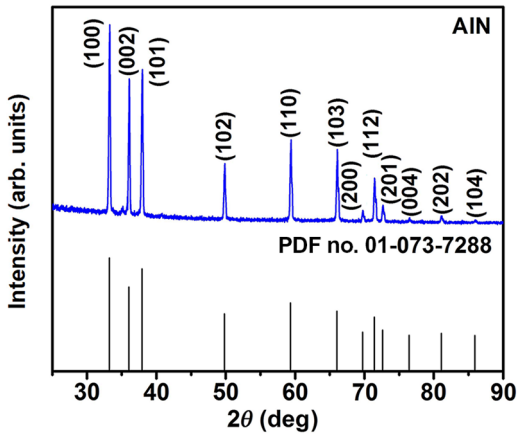

FIG. 7. XRD pattern of as-prepared AlN NW and standard card of AlN (PDF no. 01-073-7288).

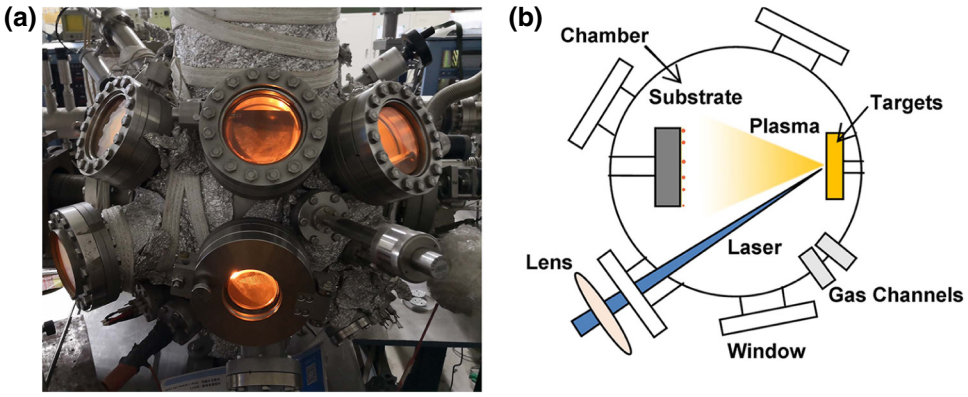

FIG. 8. (a) Photograph of PLD equipment. (b) Schematic diagram of PLD system.

for carriers are gradually intensified and, then, a reduced mobility is achieved; meanwhile, the intrinsic excitation to raise the concentration of electron-hole pairs is also gradually enhanced. Take AlN NW, for instance, when the temperature is close to 300 K, the scattering of the lattice vibration is predominant and slightly decreases the photocurrent of AlN NW. At 373 K, the contribution from intrinsic excitation exceeds the lattice vibration, resulting in a significant increase in photocurrent. However, for the AlN NW-NiO QD material, intrinsic excitation dominates throughout the temperature range. The response speed at various temperatures is presented in Figs. 5(b) and 12(c)–12(e) (see Appendix D); the mean parameters of multiple measurements are listed in Table II. Distinctly, both the rise and decay times for AlN NW and the rise time for the AlN NW-NiO QD material are insensitive to temperature, exhibiting excellent high-temperature adaptability, although the decay time of the AlN NW-NiO QD material increases significantly due to the lower recombination rate of electron-hole pairs at high temperature [47]. Notably, this is still a very fast response speed among AlN-based photoconductive photodetectors (Table I), revealing the promising performance of both AlN NW and AlN NW-NiO QD based VUV photodetectors at high temperature.

In addition, for a typical application in an irradiation environment, the VUV photodetectors are required to withstand a radiation atmosphere composed of galactic cosmic rays [48,49] and solar cosmic rays [50], in which the high-energy protons and electrons will disable the photodetectors by introducing irradiation damage. In this study, the performance of AlN NW [Figs. 5(c)–5(e)] and the AlN NW-NiO QD material [Figs. 5(f)–5(h)], after irradiation by 170 keV electrons and 120 keV protons, with doses ranging from 10^{13} to 10^{15} cm^{-2}, are measured. Only a slightly decrease in photocurrent for AlN NW after both electron [from (8.47 ± 0.31) to (6.06 ± 0.18) nA, Fig. 5(c)] and proton irradiation [from (8.47 ± 0.31) to (5.18 ± 0.12) nA, Fig. 5(d)] indicates the excellent radiation resistance of AlN NW to the irradiation environment. In general, the energy spectrum for protons in the low earth orbit ranges from 100 keV to 400 MeV, while that for electrons ranges from 40 keV to 7 MeV. Additionally, the maximum flux is 10^5 cm^{-2} s^{-1} for proton irradiation and 5×10^6 cm^{-2} s^{-1} for electron irradiation [51]. Here, AlN NW can endure the 120 keV protons with 10^{15} cm^{-2} and 170 keV electrons with 10^{15} cm^{-2}. Hence, AlN NW is able to consistently work beyond 35 days under proton irradiation and at least 55 days under electron irradiation, without any protection. The rise time for AlN NW [Fig. 5(e)] after proton irradiation basically remains unchanged (around 22.5 ms) as a function of the dose, while, after electron irradiation, the rise time decreases from (28 ± 5.5) ms (10^{13} cm^{-2}) to (15 ± 6) ms (10^{14} cm^{-2}) and then increases to (28.5 ± 7.5) ms (10^{15} cm^{-2}). Similarly, after proton irradiation, the decay time shows no clear changes (around 22.5 ms) with an increase in irradiation dose and after electron irradiation, and thus, the characteristics of first lowering and then raising the decay time can be clearly observed [(35 ± 7.5) ms (10^{13} cm^{-2}), (20 ± 7) ms (10^{14} cm^{-2}), and (27.5 ± 8.5) ms (10^{15} cm^{-2})]. The response speed of AlN NW under different V_{DS} has a similar trend after

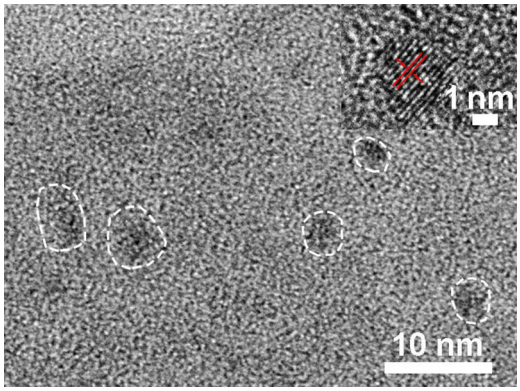

FIG. 9. TEM and HRTEM images (inset) of NiO QDs for a deposition of 10 min.

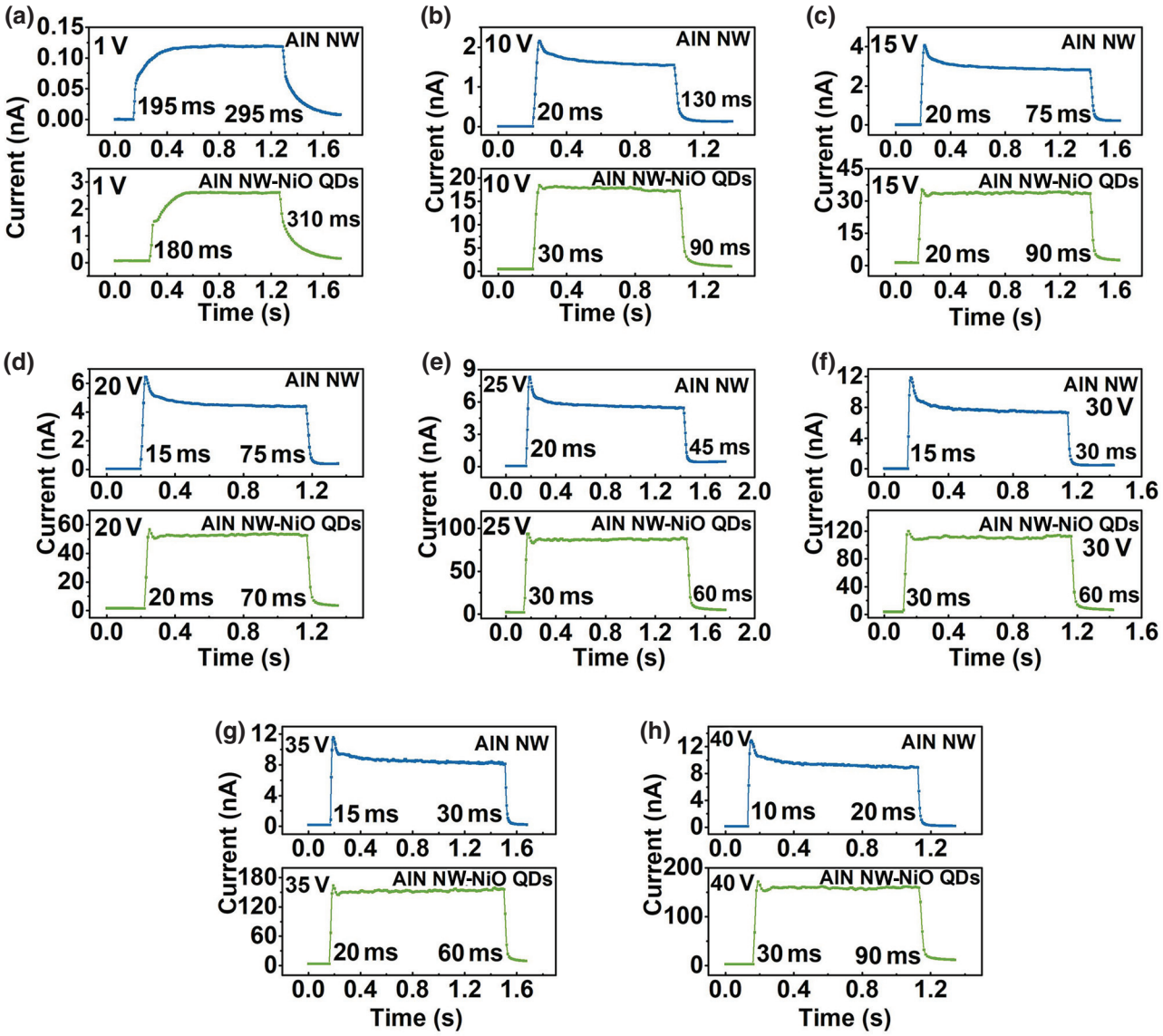

FIG. 10. Time-dependent AlN NW (top) and AlN NW-NiO QD material (bottom) photodetectors under bias voltages of (a) 1 V, (b) 10 V, (c) 15 V, (d) 20 V, (e) 25 V, (f) 30 V, (g) 35 V, and (h) 40 V.

irradiation (Fig. 13 in Appendix D). In contrast, both electron and proton irradiation have an apparent impact on the AlN NW-NiO QD material. As shown in Fig. 5(f), after electron irradiation, the photocurrent rapidly decreases from (216.39 ± 5.5) nA (pristine) to (115.52 ± 3.53) nA (10^{13} cm^{-2}), and then further reduces to (24.69 ± 0.75) nA (10^{14} cm^{-2}) and (14.54 ± 0.50) nA (10^{15} cm^{-2}). After proton irradiation [Fig. 5(g)], the photocurrent initially significantly decreases from (216.39 ± 5.5) nA (pristine) to (22.37 ± 0.65) nA (10^{13} cm^{-2}) and then slowly reduces to (17.73 ± 0.50) nA (10^{14} cm^{-2}) and (15.26 ± 0.50) nA (10^{15} cm^{-2}). Additionally, as for electron irradiation, the response speed of the AlN NW-NiO QD material generally increases with the dose, while, as for proton irradiation, the rise time shows no clear changes (around 25 ms), but the decay time increases from (32.5 ± 7) ms (10^{13} cm^{-2}) to (56.7 ± 9.5) ms (10^{15} cm^{-2}) as a function of the dose [Fig. 5(h)]. The response speed of the AlN NW-NiO QD material at different V_{DS} after irradiation is shown in Fig. 14 in Appendix D. Apparently, the performance deterioration in the AlN NW-NiO QD material should be ascribed to serious damage to the NiO QDs induced by electron or proton irradiation. Herein, electron radiation mainly causes the cumulative ionizing radiation effect that builds up to trap charges in the oxide (NiO QDs) [52] and increases the number of interface traps, which will reduce the carrier concentration and accelerate the electron-hole pairs recombination rate [53]. Thus, the photocurrent of the AlN NW-NiO QD material gradually decreases with an increase in electron irradiation dose. Compared with

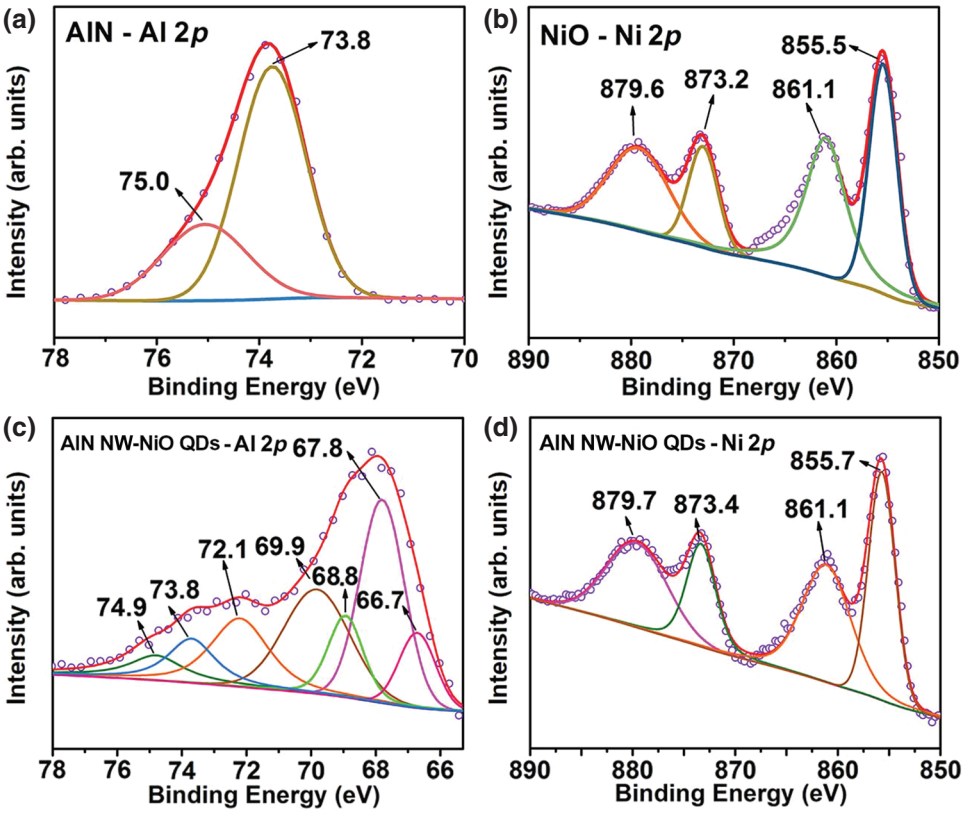

FIG. 11. XPS core-level spectra of (a) Al 2*p* of pristine AlN NW, (b) Ni 2*p* of NiO QDs, and (c) Al 2*p* and (d) Ni 2*p* of AlN NW with NiO QDs.

electron irradiation, proton irradiation induces both the ionizing radiation effect and displacement damage effect [54–56], which will introduce more destructive effects into the target, especially the latter one, causing lots of vacancies and interstitials in the lattice [57,58]. The as-generated defects easily form disordered clusters (regions), in which a large quantity of charges are trapped, and thus, reduce the photocurrent significantly [55,59,60]. So, the proton irradiation process weakens the performance of the AlN NW-NiO QD material, which approaches that of AlN NW, even at a low dose, as expected. Hence, the AlN NW-NiO QD material can endure 170 keV electron irradiation with a dose of 10^{13} cm^{-2} and its estimated lifetime is only 14 h under electron irradiation without any protection. By far, these aforementioned experiments convincingly demonstrate an AlN-based VUV photodetector with excellent photoelectric properties and an outstanding enhancement after NiO decoration. Further evaluation of the irradiation environment proves the excellent resistance of AlN-based VUV photodetectors towards both electron and proton bombardment and reveals the promising potential of AlN NW-NiO QD based VUV photodetectors under low-dose electron irradiation. In the future, research to probe the protective strategy for current NiO QDs, or searches for another *p*-type semiconductor that could withstand high-dose proton irradiation, are expected to further promote the design and development of VUV-based devices, especially in the special environment of space.

III. CONCLUSION

In summary, a mixed-dimensional strategy is utilized to construct AlN NW-NiO QD based VUV photodetectors via the PLD technique. The synergic action of the heterostructure and built-in electric field increases the photogenerated electron concentration in AlN NW and the separation efficiency of the photoexcited electron-hole pairs, which results in an excellent enhancement of the carrier concentration. Furthermore, the AlN NW-NiO QD material achieves a series of significant performance improvements compared with that of other AlN-based photodetectors, including an ultrahigh photoconductive gain (9.96), high light-to-dark ratios (3.6×10^5), excellent detectivity (5×10^6 Jones), and high response speeds ($R_t < 30$ ms and $D_t < 90$ ms). In addition, irradiation experiments show that the AlN NW-NiO QD material can withstand a certain dose of electron irradiation, but is very sensitive to proton irradiation due to the instability of NiO QDs. By contrast, the AlN NW exhibit great potential in an irradiation environment. This work also affords an insight into the design and fabrication of WBGS-based VUV optoelectronic devices for other special applications.

ACKNOWLEDGMENTS

This work is supported by the National Natural Science Foundation of China (Grants No. 51372056, No. 51672057, No. 51722205, No. 51772064, and No.

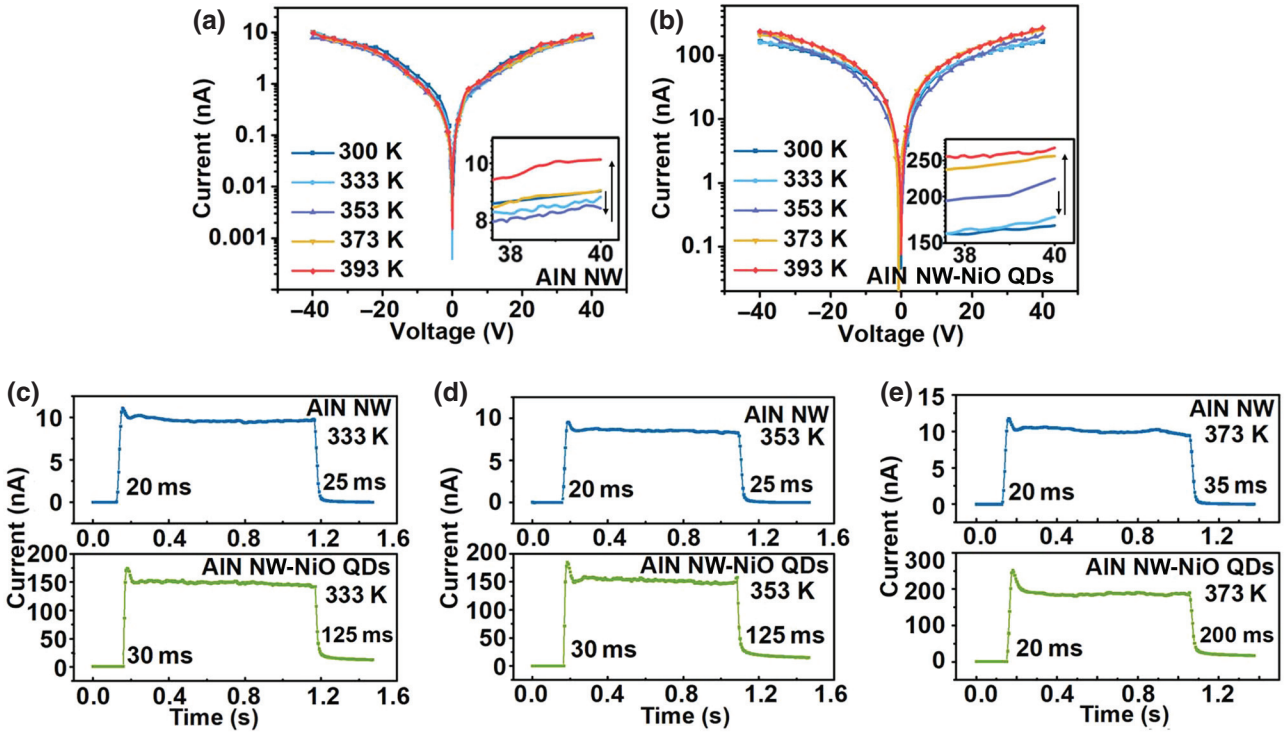

FIG. 12. (a) Semilogarithmic *I-V* characteristics of AlN NW at high temperature, ranging from 300 to 393 K, under illumination of 193 nm. Inset shows an enlarged image of the *I-V* curves from 38–40 V to clearly illustrate the variation of photocurrent at different high temperatures. (b) Semilogarithmic *I-V* characteristics of AlN NW-NiO QD material at high temperature, ranging from 300 to 393 K, under illumination of 193 nm. Inset shows an enlarged image of the *I-V* curves from 38 to 40 V to clearly illustrate the variation of photocurrent at different high temperatures. (c)–(e) Time-dependent photoresponses of AlN NW (top) and AlN NW-NiO QD (bottom) photodetectors over the range of 333–373 K.

51772067), the Foundation for Innovative Research Groups of the National Natural Science Foundation of China (Grant No. 11421091), the International Science & Technology Cooperation Program of China (Grant No. 2012DFR50020), the Fundamental Research Funds for the Central Universities (Grant No. HIT.BRETIV.201801), the Natural Science Foundation of Heilongjiang Province (Grant No. E2018032), the Science and Technology Project of Shenzhen (Grant No. JCYJ 2016050611 3431828), and the Program for New Century Excellent Talents in University (Grant No. NCET-13-0174).

APPENDIX A: SYNTHESIS AND XRD CHARACTERISTICS OF AlN NWs

The experimental details of preparing AlN NWs are presented as follows. A quantity of 25 g of high-purity AlN powder (99.999%, Alfa-Aesar) is inserted into a tantalum carbide (TaC) crucible. Successively, the TaC crucible is centered in a graphite crucible. This installation is transferred into a homemade radiofrequency-heated furnace, generating 12 kW (Fig. 6). Initially, the furnace is evacuated to a pressure lower than 3×10^{-3} Pa and, then, high-purity N_2 (99.9999%) is inserted into the chamber until a pressure of about 1×10^5 Pa is reached. To eliminate oxygen, this process is carried out at least three times. Then, the N_2 pressure is maintained at approximately $6.5–8 \times 10^4$ Pa. The temperature is raised from room temperature to 1900–1950 °C at a rate of 22–26 °C/min and kept at the target temperature for 30–45 min. After the reaction occurs, a N_2 (99.999%) flow of 500–700 standard cubic centimeter per minute (sccm) is injected into the furnace to accelerate the cooling process. The samples are then collected from the surface of the TaC lid and characterized.

Figure 7 shows the XRD pattern of the AlN NWs with the standard ICDD-PDF-2 card no. 01-073-7288 for comparison.

APPENDIX B: SYNTHESIS AND TEM CHARACTERISTICS OF NiO QDs

The experimental details of decorating NiO QDs onto AlN NW are presented as follows. First, 2 g of NiO powder (99%, Alfa-Aesar) is compressed into an 11 mm diameter round disk. NiO is sintered into a muffle furnace via a solid-state reaction carried out at 873 K for 2 h. Subsequently, the NiO target is fixed at the target position in the

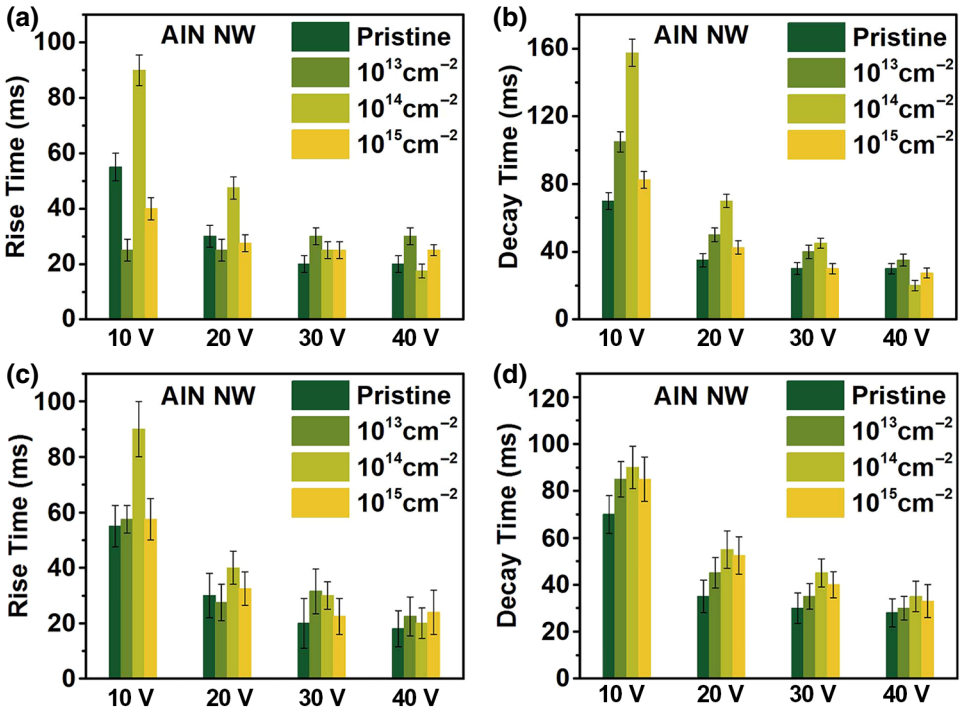

FIG. 13. Response speed of AlN NW under different V_{DS} after (a),(b) 170 keV electron irradiation and (c),(d) 120 keV proton irradiation.

chamber via PLD (Fig. 8). The AlN NW are inserted into the chamber and attached to the substrate. The chamber is then evacuated to reach a pressure of 10^{-3} Pa. The chamber is filled with 15 Pa high-purity oxygen (99.9999%) during the experimental process to maintain an oxygen-rich atmosphere, which is needed to produce the p-type NiO QDs. Successively, a KrF laser with a wavelength of 248 nm and a repetition rate of 1 Hz is pulsed through a lens with a 30 cm focal length and focused onto the NiO target. This process produced a large amount of plume, which is deposited onto the AlN NW for 10 min. Finally, the AlN NW-NiO QD material are annealed at 400 °C to obtain fine crystalline NiO QDs. It is found that, if we further increase the deposition time, the previously deposited NiO QDs will merge with the surrounding QDs to form a thin NiO film. Similar phenomena are observed in the growth of other types of QDs by the PLD technique [61,62].

Figure 9 and inset show the TEM and HRTEM images of isolated NiO QDs, respectively, which are marked by white dashed lines.

APPENDIX C: MATERIAL CHARACTERIZATION, DEVICE FABRICATION, AND MEASUREMENTS

The size and morphology of the samples are characterized by using a scanning electron microscope (Thermo Scientific Apreo C) and a transmission electron microscope (JEM-1200EX) equipped with an energy-dispersive X-ray analyzer. The crystal structure of the products is analyzed by employing a confocal Raman spectroscopy system (JY-HR800, with <0.9 cm^{-1} distinguishability and 10 μm spot diameter) and an X-ray photoelectron spectrometer (Thermo Escalab 250XI). The energy gap of NiO is measured by recording a PL spectrum with a Hitachi F-4500 fluorescence spectrophotometer.

The fabrication method of AlN NW-NiO QD -based photodetectors via photolithography process is discussed in detail herein and shown in Figs. 2(a)–2(e). The I-V characteristic curves and the photoelectric response of the AlN NW or AlN NW-NiO QD material are measured in air at room temperature by using a CRYOX80 vacuum low-temperature probe station (SWIN) with a Keithley 6517B current test system. The response speed of the devices is measured by employing a Keithley 2602B system source meter. The illumination source, with a wavelength of 193 nm, is produced by an Excistar XS-type excimer laser (Coherent) by exciting ArF gas. The high-temperature test is realized by heating the platform of probe station. The electron and proton irradiation is performed by using the $\mathcal{KH}\Phi\mathcal{K}$ simulator of space electron (proton) radiation at 300 K. The sample is placed on a rotating state in a vacuum chamber of 10^{-4} Pa and bombarded by the irradiation vertically. All of the results collected at high temperature and electron-proton irradiation are obtained by averaging more than three times.

APPENDIX D: SUPPLEMENTAL CHARACTERISTICS DATA

The time-dependent results of AlN NW and AlN NW-NiO QD material under different bias (from 1 to 10 V) are shown in Fig. 10.

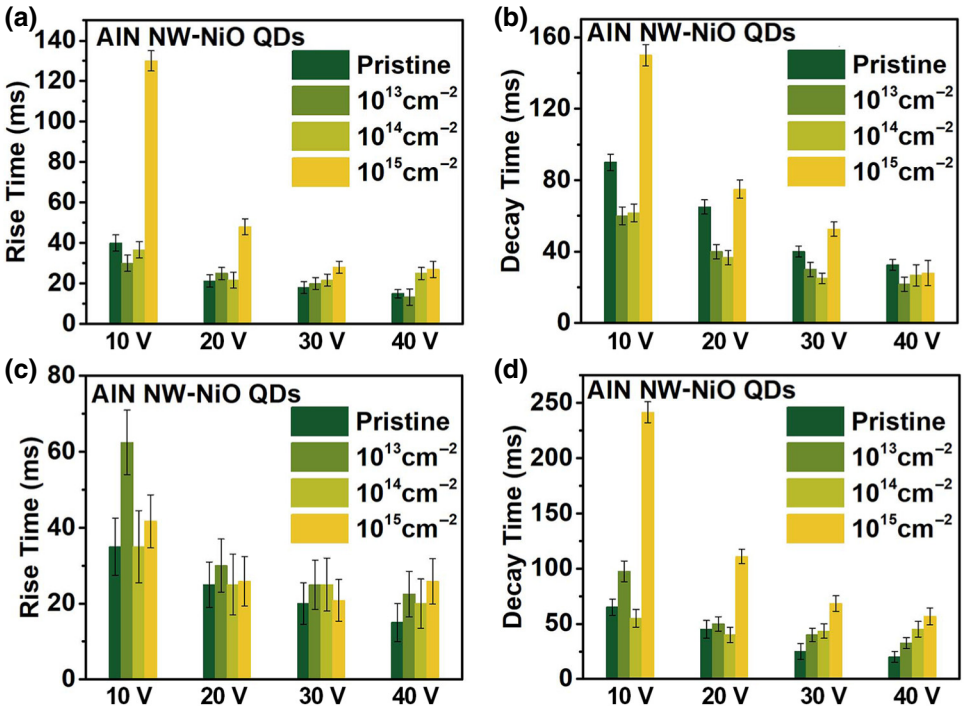

FIG. 14. Response speed of AlN NW-NiO QD material under different V_{DS} after (a),(b) 170 keV electron irradiation and (c),(d) 120 keV proton irradiation.

Clearly, the Al 2*p* CL spectrum of AlN NW [Fig. 11(a)] can be fitted by two peaks located at 73.8 and 75.0 eV, which are attributed to the Al—N and Al—O bonds, respectively [63]. The Al 2*p* CL spectrum of the AlN NW-NiO QD material [Fig. 11(c)] presents these two same transitions at 73.8 and 74.9 eV, respectively. Moreover, the CL peak located at 72.1 eV corresponds to the Al—Ni bond, while the other features, which are present in the 69.9–66.7 eV region, are attributed to the partial overlap of the Ni 3*p* level with the Al 2*p* one [64]. In addition, the Ni 2*p* CL spectrum of the isolated NiO QDs [Fig. 11(b)] can be resolved into four peaks, corresponding to the Ni—O bond (855.5 and 873.2 eV) and its satellite peaks (879.6 and 861.1 eV) [65], and its binding energy is similar to the AlN NW-NiO QD material [Fig. 11(d)].

Figure 12 presents the *I*-*V* characteristics and response speeds of AlN NW and the AlN NW-NiO QD material at various high temperatures ranging from 300 to 393 K.

Figures 13 and 14 show the response speeds of AlN NW and the AlN NW-NiO QD material at different V_{DS}, respectively, which are irradiated by 170 keV electrons and 120 keV protons with various doses ranging from 10^{13} to 10^{15} cm^{-2}.

[1] B. Zhao, F. Wang, H. Chen, L. Zheng, L. Su, D. Zhao, and X. Fang, An ultrahigh responsivity (9.7mA W^{-1}) self-powered solar-blind photodetector based on individual ZnO-Ga_2O_3 heterostructures, Adv. Funct. Mater. **27**, 1700264 (2017).

[2] W. Ouyang, F. Teng, and X. Fang, High performance BiOCl nanosheets/TiO_2 nanotube arrays heterojunction UV photodetector: The influences of self-induced inner electric fields in the BiOCl nanosheets, Adv. Funct. Mater. **28**, 1707178 (2018).

[3] Y. Jin, J. Wang, B. Sun, J. C. Blakesley, and N. C. Greenham, Solution-processed ultraviolet photodetectors based on colloidal ZnO nanoparticles, Nano Lett. **8**, 1649 (2008).

[4] Y. Q. Bie, Z. M. Liao, H. Z. Zhang, G. R. Li, Y. Ye, Y. B. Zhou, J. Xu, Z. X. Qin, L. Dai, and D. P. Yu, Self-powered, ultrafast, visible-blind UV detection and optical logical operation based on ZnO/GaN nanoscale p-n junctions, Adv. Mater. **23**, 649 (2011).

[5] S. M. Hatch, J. Briscoe, and S. Dunn, A self-powered ZnO-nanorod/CuSCN UV photodetector exhibiting rapid response, Adv. Mater. **25**, 867 (2013).

[6] L. Ondic, K. Dohnalova, M. Ledinsky, A. Kromka, O. Babchenko, and B. Rezek, Effective extraction of photoluminescence from a diamond layer with a photonic crystal, ACS Nano **5**, 346 (2011).

[7] D.-Y. Guo, P.-G. Li, Z.-W. Chen, Z.-P. Wu, and W.-H. Tang, Ultra-wide bandgap semiconductor of β-Ga_2O_3 and its research progress of deep ultraviolet transparent electrode and solar-blind photodetector, Acta Phys. Sin. **68**, 078501 (2019).

[8] B. Sun, Y. Sun, and C. Wang, Flexible transparent and free-standing SiC nanowires fabric: Stretchable UV absorber and fast-response UV-A detector, Small **14**, e1703391 (2018).

[9] F. Gonzalez-Posada, R. Songmuang, M. Den Hertog, and E. Monroy, Room-temperature photodetection dynamics of single GaN nanowires, Nano Lett. **12**, 172 (2012).

[10] C. Soci, A. Zhang, B. Xiang, S. A. Dayeh, D. P. R. Aplin, J. Park, X. Y. Bao, Y. H. Lo, and D. Wang, Zno nanowire UV photodetectors with high internal gain, Nano Lett. **7**, 1003 (2007).

[11] Z. Wang, R. Yu, C. Pan, Z. Li, J. Yang, F. Yi, and Z. L. Wang, Light-induced pyroelectric effect as an effective approach for ultrafast ultraviolet nanosensing, Nat. Commun. **6**, 8401 (2015).

[12] X. Liu, L. Gu, Q. Zhang, J. Wu, Y. Long, and Z. Fan, All-printable band-edge modulated ZnO nanowire photodetectors with ultra-high detectivity, Nat. Commun. **5**, 4007 (2014).

[13] Y. Taniyasu, M. Kasu, and T. Makimoto, An aluminium nitride light-emitting diode with a wavelength of 210 nanometres, Nature **441**, 325 (2006).

[14] P. Perry and R. Rutz, The optical absorption edge of single-crystal AlN prepared by a close-spaced vapor process, Appl. Phys. Lett. **33**, 319 (1978).

[15] L. Jin, H. Zhang, R. Pan, P. Xu, J. Han, X. Zhang, Q. Yuan, Z. Zhang, X. Wang, Y. Wang, and B. Song, Observation of the long afterglow in AlN helices, Nano Lett. **15**, 6575 (2015).

[16] A. BenMoussa, A. Soltani, J.-C. Gerbedoen, T. Saito, S. Averin, S. Gissot, B. Giordanengo, G. Berger, U. Kroth, and J.-C. De Jaeger, Developments, characterization and proton irradiation damage tests of AlN detectors for VUV solar observations, Nucl. Instrum. Methods Phys. Res., Sect. B. **312**, 48 (2013).

[17] C. Xie, X.-T. Lu, X.-W. Tong, Z.-X. Zhang, F.-X. Liang, L. Liang, L.-B. Luo, and Y.-C. Wu, Recent progress in solar-blind deep-ultraviolet photodetectors based on inorganic ultrawide bandgap semiconductors, Adv. Funct. Mater. **29**, 1806006 (2019).

[18] Y.-B. Tang, X.-H. Bo, J. Xu, Y.-L. Cao, Z.-H. Chen, H.-S. Song, C.-P. Liu, T.-F. Hung, W.-J. Zhang, H.-M. Cheng, I. Bello, S.-T. Lee, and C.-S. Lee, Tunable p-type conductivity and transport properties of AlN nanowires via Mg doping, ACS Nano **5**, 3591 (2011).

[19] M. Spies, M. I. den Hertog, P. Hille, J. Schormann, J. Polaczynski, B. Gayral, M. Eickhoff, E. Monroy, and J. Lahnemann, Bias-controlled spectral response in GaN/AlN single-nanowire ultraviolet photodetectors, Nano Lett. **17**, 4231 (2017).

[20] D. Zhang, Z. Liu, C. Li, T. Tang, X. Liu, S. Han, B. Lei, and C. Zhou, Detection of NO_2 down to ppb levels using individual and multiple In_2O_3 nanowire devices, Nano Lett. **4**, 1919 (2004).

[21] Y. Ning, Z. Zhang, F. Teng, and X. Fang, Novel transparent and self-powered UV photodetector based on crossed ZnO nanofiber array homojunction, Small **14**, e1703754 (2018).

[22] D. Nam, D. S. Sukhdeo, J. H. Kang, J. Petykiewicz, J. H. Lee, W. S. Jung, J. Vuckovic, M. L. Brongersma, and K. C. Saraswat, Strain-induced pseudoheterostructure nanowires confining carriers at room temperature with nanoscale-tunable band profiles, Nano Lett. **13**, 3118 (2013).

[23] M. C. McAlpine, H. Ahmad, D. Wang, and J. R. Heath, Highly ordered nanowire arrays on plastic substrates for ultrasensitive flexible chemical sensors, Nat. Mater. **6**, 379 (2007).

[24] J. Xu, X. Zhuang, P. Guo, Q. Zhang, W. Huang, Q. Wan, W. Hu, X. Wang, X. Zhu, C. Fan, Z. Yang, L. Tong, X. Duan, and A. Pan, Wavelength-converted/selective waveguiding based on composition-graded semiconductor nanowires, Nano Lett. **12**, 5003 (2012).

[25] W. Zheng, F. Huang, R. Zheng, and H. Wu, Low-dimensional structure vacuum-ultraviolet-sensitive ($\lambda <$ 200 nm) photodetector with fast-response speed based on high-quality AlN micro/nanowire, Adv. Mater. **27**, 3921 (2015).

[26] M. S. Gudiksen, L. J. Lauhon, J. Wang, D. C. Smith, and C. M. Lieber, Growth of nanowire superlattice structures for nanoscale photonics and electronics, Nature **415**, 617 (2002).

[27] X. He, X. Wang, S. Nanot, K. Cong, Q. Jiang, A. A. Kane, J. E. M. Goldsmith, R. H. Hauge, F. Léonard, and J. Kono, Photothermoelectric p–n junction photodetector with intrinsic broadband polarimetry based on macroscopic carbon nanotube films, ACS Nano **7**, 7271 (2013).

[28] K. Yan, D. Wu, H. Peng, L. Jin, Q. Fu, X. Bao, and Z. Liu, Modulation-doped growth of mosaic graphene with single-crystalline p-n junctions for efficient photocurrent generation, Nat. Commun. **3**, 1280 (2012).

[29] N. H. Tran, B. H. Le, S. Zhao, and Z. Mi, On the mechanism of highly efficient p-type conduction of Mg-doped ultra-wide-bandgap AlN nanostructures, Appl. Phys. Lett. **110**, 032102 (2017).

[30] L. Li, L. Gu, Z. Lou, Z. Fan, and G. Shen, Zno quantum dot decorated Zn_2SnO_4 nanowire heterojunction photodetectors with drastic performance enhancement and flexible ultraviolet image sensors, ACS Nano **11**, 4067 (2017).

[31] D. Y. Kim, J. Ryu, J. Manders, J. Lee, and F. So, Air-stable, solution-processed oxide p-n heterojunction ultraviolet photodetector, ACS Appl. Mater. Inter. **6**, 1370 (2014).

[32] W. Yan, Z. Sun, Z. Li, Q. Liu, T. Yao, Z. Pan, C. Wang, F. Hu, Y. Jiang, Z. Qi, F. Zeng, and S. Wei, Valence state-dependent ferromagnetism in Mn-doped NiO thin films, Adv. Mater. **24**, 353 (2012).

[33] S. Ghosh, M. Baral, R. Kamparath, R. J. Choudhary, D. M. Phase, S. D. Singh, and T. Ganguli, Epitaxial growth and interface band alignment studies of all oxide α-Cr_2O_3/β-Ga_2O_3 p-n heterojunction, Appl. Phys. Lett. **115**, 061602 (2019).

[34] C. Lu, L. Qi, J. Yang, X. Wang, D. Zhang, J. Xie, and J. Ma, One-Pot synthesis of octahedral Cu_2O nanocages via a catalytic solution route, Adv. Mater. **17**, 2562 (2005).

[35] A. Liu, H. Zhu, Z. Guo, Y. Meng, G. Liu, E. Fortunato, R. Martins, and F. Shan, Solution combustion synthesis: Low-temperature processing for p-type Cu:NiO thin films for transparent electronics, Adv. Mater. **29**, 1701599 (2017).

[36] J. Rodríguez-Carvajal, Introduction to the program FULLPROF: refinement of crystal and magnetic structures from powder and single crystal data, (2001).

[37] V. Y. Davydov, Y. E. Kitaev, I. N. Goncharuk, A. N. Smirnov, J. Graul, O. Semchinova, D. Uffmann, M. B. Smirnov, A. P. Mirgorodsky, and R. A. Evarestov, Phonon dispersion and Raman scattering in hexagonal GaN and AlN, Phys. Rev. B **58**, 12899 (1998).

[38] F. Yang, L. Jin, L. Sun, X. Ren, X. Duan, H. Cheng, Y. Xu, X. Zhang, Z. Lai, W. Chen, H. Dong, and W. Hu, Free-standing 2D hexagonal aluminum nitride dielectric crystals for high-performance organic field-effect transistors, Adv. Mater. **30**, e1801891 (2018).

[39] M. Patel, J. Kim, B. S. Kim, Y.-H. Kim, and J. Kim, Optical and photoelectrochemical properties of transparent NiO quantum dots, Mater. Lett. **218**, 123 (2018).

[40] D. Guo, Y. Su, H. Shi, P. Li, N. Zhao, J. Ye, S. Wang, A. Liu, Z. Chen, C. Li, and W. Tang, Self-Powered ultraviolet photodetector with superhigh photoresponsivity (3.05A/W) based on the GaN/Sn:Ga_2O_3 pn junction, ACS Nano **12**, 12827 (2018).

[41] L. Ma, W. Hu, Q. Zhang, P. Ren, X. Zhuang, H. Zhou, J. Xu, H. Li, Z. Shan, X. Wang, L. Liao, H. Q. Xu, and A. Pan, Room-temperature near-infrared photodetectors based on single heterojunction nanowires, Nano Lett. **14**, 694 (2014).

[42] Q. Yang, X. Guo, W. Wang, Y. Zhang, S. Xu, D. H. Lien, and Z. L. Wang, Enhancing sensitivity of a single ZnO micro-/nanowire photodetector by piezo-phototronic effect, ACS Nano **4**, 6285 (2010).

[43] R. Saran and R. J. Curry, Lead sulphide nanocrystal photodetector technologies, Nat. Photonics **10**, 81 (2016).

[44] T. Yang, B. Zheng, Z. Wang, T. Xu, C. Pan, J. Zou, X. Zhang, Z. Qi, H. Liu, Y. Feng, W. Hu, F. Miao, L. Sun, X. Duan, and A. Pan, Van der waals epitaxial growth and optoelectronics of large-scale WSe_2/SnS_2 vertical bilayer p-n junctions, Nat. Commun. **8**, 1906 (2017).

[45] M. H. Chiu, C. Zhang, H. W. Shiu, C. P. Chuu, C. H. Chen, C. Y. Chang, C. H. Chen, M. Y. Chou, C. K. Shih, and L. J. Li, Determination of band alignment in the single-layer MoS_2/WSe_2 heterojunction, Nat. Commun. **6**, 7666 (2015).

[46] D. Guo, K. Chen, S. Wang, F. Wu, A. Liu, C. Li, P. Li, C. Tan, and W. Tang, Self-powered Solar-Blind Photodetectors Based on α/β Phase Junction of Ga_2O_3, Phys. Rev. Appl. **13**, 024051 (2020).

[47] S. Ghosh, I. Calizo, D. Teweldebrhan, E. P. Pokatilov, D. L. Nika, A. A. Balandin, W. Bao, F. Miao, and C. N. Lau, Extremely high thermal conductivity of graphene: Prospects for thermal management applications in nanoelectronic circuits, Appl. Phys. Lett. **92**, 151911 (2008).

[48] V. A. Acciari, E. Aliu, T. Arlen, T. Aune, M. Bautista, M. Beilicke, W. Benbow, D. Boltuch, S. M. Bradbury, J. H. Buckley, *et al.*, A connection between star formation activity and cosmic rays in the starburst galaxy M82, Nature **462**, 770 (2009).

[49] S. Buitink, A. Corstanje, H. Falcke, J. R. Hörandel, T. Huege, A. Nelles, J. P. Rachen, L. Rossetto, P. Schellart, O. Scholten, *et al.*, A large light-mass component of cosmic rays at 1017–1017.5 electronvolts from radio observations, Nature **531**, 70 (2016).

[50] S. D. Bale, S. T. Badman, J. W. Bonnell, T. A. Bowen, D. Burgess, A. W. Case, C. A. Cattell, B. D. G. Chandran, C. C. Chaston, C. H. K. Chen, *et al.*, Highly structured slow solar wind emerging from an equatorial coronal hole, Nature **576**, 237 (2019).

[51] T. Vogl, K. Sripathy, A. Sharma, P. Reddy, J. Sullivan, J. R. Machacek, L. Zhang, F. Karouta, B. C. Buchler, and M. W. Doherty, Radiation tolerance of two-dimensional material-based devices for space applications, Nat. Commun. **10**, 1 (2019).

[52] J. Zang, L. Bao, R. A. Webb, and X. Li, Electron beam irradiation stiffens zinc tin oxide nanowires, Nano Lett. **11**, 4885 (2011).

[53] X. Yu, Y. Shen, T. Liu, T. T. Wu, and Q. Jie Wang, Photocurrent generation in lateral graphene p-n junction created by electron-beam irradiation, Sci. Rep. **5**, 12014 (2015).

[54] R. A. Miller, H. So, H. C. Chiamori, K. M. Dowling, Y. Wang, and D. G. Senesky, Graphene-enhanced gallium nitride ultraviolet photodetectors under 2 MeV proton irradiation, Appl. Phys. Lett. **111**, 241902 (2017).

[55] S. Xue, R. Huang, P. Wang, W. Wang, D. Wu, Y. Pei, and X. Zhang, Impact of proton-radiation-induced spacer damage on the dc characteristics degradation in deep-submicron metal-oxide-semiconductor field effect transistors, J. Appl. Phys. **105**, 084505 (2009).

[56] S.-F. Tang, H.-H. Hsieh, H.-Y. Tu, T.-H. You, S.-Y. Lin, L.-C. Wang, and C.-D. Chiang, Investigations for InAs/GaAs multilayered quantum-dot structure treated by high energy proton irradiation, Thin Solid Films **518**, 7425 (2010).

[57] B. Park, D. Ho, G. Kwon, D. Kim, S. Y. Seo, C. Kim, and M.-G. Kim, Solution-Processed Rad-hard amorphous metal-oxide thin-film transistors, Adv. Funct. Mater. **28**, 1802717 (2018).

[58] R.-W. Zhou, X.-C. Liu, H.-J. Wang, W.-B. Chen, F. Li, S.-Y. Zhuo, and E.-W. Shi, Ferromagnetism in proton irradiated 4H-SiC single crystal, AIP Adv. **5**, 047146 (2015).

[59] S. M. Khanna, J. Webb, H. Tang, A. J. Houdayer, and C. Carlone, 2MeV proton radiation damage studies of gallium nitride films through low temperature photoluminescence spectroscopy measurements, IEEE Trans. Nucl. Sci. **47**, 2322 (2000).

[60] Y.-K. Moon, S. Lee, D.-Y. Moon, W.-S. Kim, B.-W. Kang, and J.-W. Park, Effects of proton irradiation on indium zinc oxide-based thin-film transistors, Surf. Coat. Technol. **205**, S109 (2010).

[61] J. Li, Y. Zhang, T. Gao, C. Hu, T. Yao, Q. Yuan, X. Wang, P. Xu, Z. Zhang, J. Jian, X. Zhang, and B. Song, Quantum dot-induced improved performance of cadmium telluride (CdTe) solar cells without a Cu buffer layer, J. Mater. Chem. A **5**, 4904 (2017).

[62] K. Fujisawa, I. Ka, V. Le Borgne, C.-S. Kang, K. Kobayashi, H. Muramatsu, T. Hayashi, Y. A. Kim, M. Endo, M. Terrones, and M. A. El Khakani, Elucidating the local interfacial structure of highly photoresponsive carbon nanotubes/PbS-QDs based nanohybrids grown by pulsed laser deposition, Carbon **96**, 145 (2016).

[63] H. Y. Chen, H. L. Lu, J. X. Chen, F. Zhang, X. M. Ji, W. J. Liu, X. F. Yang, and D. W. Zhang, Low-Temperature One-step growth of AlON thin films with homogenous nitrogen-doping profile by plasma-enhanced atomic layer deposition, ACS Appl. Mater. Inter. **9**, 38662 (2017).

[64] M. Jarosz, R. P. Socha, P. Jóźwik, and G. D. Sulka, Amperometric glucose sensor based on the $Ni(OH)_2/Al(OH)_4$ - electrode obtained from a thin Ni_3Al foil, Appl. Surf. Sci. **408**, 96 (2017).

[65] C. Xuan, J. Wang, W. Xia, Z. Peng, Z. Wu, W. Lei, K. Xia, H. L. Xin, and D. Wang, Porous structured Ni-Fe-P nanocubes derived from a prussian blue analogue as an electrocatalyst for efficient overall water splitting, ACS Appl. Mater. Inter. **9**, 26134 (2017).

[66] G. Liu, C. Yan, G. Zhou, Z. Qin, Q. Zhou, R. Zheng, H. Wu, and Z. Sun, Defects induced broad spectral photoresponse of PVT-grown bulk AlN crystals, Scr. Mater. **154**, 45 (2018).

[67] R. Dahal, T. Al Tahtamouni, Z. Fan, J. Lin, and H. Jiang, Hybrid AlN-SiC deep ultraviolet schottky barrier photodetectors, Appl. Phys. Lett. **90**, 263505 (2007).

[68] S. Nikishin, B. Borisov, M. Pandikunta, R. Dahal, J.-Y. Lin, H. X. Jiang, H. Harris, and M. Holtz, High quality AlN for deep UV photodetectors, Appl. Phys. Lett. **95**, 054101 (2009).

[69] W. Zheng, R. Lin, J. Ran, Z. Zhang, X. Ji, and F. Huang, Vacuum-ultraviolet photovoltaic detector, ACS Nano **12**, 425 (2018).

[70] W. Zheng, R. Lin, D. Zhang, L. Jia, X. Ji, and F. Huang, Vacuum-Ultraviolet photovoltaic detector with improved response speed and responsivity via heating annihilation trap state mechanism, Adv. Opt. Mater. **6**, 1800697 (2018).

[71] W. Zheng, R. Lin, L. Jia, and F. Huang, Vacuum ultraviolet photovoltaic arrays, Photonics Res. **7**, 98 (2019).